RSC Advances

PAPER

View Article Online
View Journal | View Issue

Cite this: *RSC Adv.*, 2025, **15**, 9110

Modification of B-site substituted by high-valence Nb in $PrBa_{0.5}Sr_{0.5}Co_{1.5}Fe_{0.5}O_{5+\delta}$ as a highly active air electrode for solid oxide fuel cell†

Qiming Guo,[a] Songbo Li,*[a] Shengli An,[b] Runze Sun,[a] Mengyao Ren,[a] Lele Gao,[c] Zhen Yan[c] and Huihui Cao[c]

Received 30th December 2024
Accepted 5th February 2025

DOI: 10.1039/d4ra09097g

rsc.li/rsc-advances

Solid oxide fuel cells (SOFCs) are a new type of power generation technology that directly converts chemical energy into electrical energy with advantages, such as low environmental pollution and high conversion efficiency. However, these fuel cells suffer challenges, including high operating temperatures and poor stability. In this paper, $PrBa_{0.5}Sr_{0.5}Co_{1.5-x}Nb_xFe_{0.5}O_{5+\delta}$ series materials were prepared *via* the sol–gel method and applied as cathode material in SOFCs. X-ray diffraction patterns reveal that the addition of Nb to $PrBa_{0.5}Sr_{0.5}Co_{1.5}Fe_{0.5}O_{5+\delta}$ did not change its crystal structure but increased the cell volume, leading to lattice expansion and improved thermal stability. Electron paramagnetic resonance quantitative analysis was conducted on $PrBa_{0.5}Sr_{0.5}Co_{1.5-x}Nb_xFe_{0.5}O_{5+\delta}$. At 800 °C, the lowest area specific resistance (ASR) at $x = 0.04$ was 0.0336 Ω cm^2, indicating that the addition of Nb significantly improved the oxygen reduction reaction catalytic activity. The power density of the electrolyte-supported single cell increased by 110.6 mW cm^{-2}. Thus, Nb addition enhances the electrochemical performance of PBSCF cathode materials, and $PBSCFNb_{0.04}$ is a promising cathode material for SOFCs.

1. Introduction

Environmental problems, such as the energy crisis and global warming, have become increasingly prominent. Solid oxide fuel cells (SOFCs) play a crucial role in advancing future energy development and have garnered significant attention from researchers due to their cleanliness and efficiency advantages.[1] However, the high development costs and low durability of SOFCs hinder their commercialization.[2] As a vital component of SOFCs, the economic durability of the cathode is the focus of many scientific researchers. Cobalt-based materials offer advantages, such as high conductivity and low ASR, making them promising candidates for SOFC cathode materials. $PrBaCo_2O_{5+\delta}$ (PBC) demonstrates high conductivity and oxygen transport performance. This P-type conductor material exhibits a high spin state of Co ions and conductivity due to its thermal activation at low temperatures.[3] However, in high-temperature environments, Co^{4+} is reduced to Co^{3+}, and the lattice oxygen in PBC gradually detaches, resulting in the formation of oxygen vacancies and reduced conductivity. The reduction of lattice oxygen in PBC leads to a high thermal expansion coefficient (TEC) and poor thermal matching between the cathode and electrolyte, which can cause cracking or detachment.[4] Therefore, this issue significantly limits the commercial development of PBC as a SOFC cathode material.[5]

To facilitate the commercialization of PBC cathode materials, many researchers have proposed various modification methods, with doping modifications becoming a research hotspot. Park *et al.*[6] doped Sr at the Pr position of $PrCoO_{3-\delta}$, achieving a considerable conductivity improvement of 2000 S cm^{-1} at a doping concentration of 0.3. Subsequently, Lü *et al.*[4,7] and Liu *et al.*[8] doped Sr into PBC to prepare $PrBa_{0.5}Sr_{0.5}Co_2O_{5+\delta}$. This increased conductivity and improved ASR but the TEC mismatch between the cathode and electrolyte remained unchanged. The Fe-based double perovskite cathode material has low TEC and ASR values.[9] Introducing appropriate amounts of Fe into the Co-based material not only avoids affecting the ASR but may also reduce the TEC. Zou *et al.*[10] observed that Fe effectively reduces the average TEC. Bai *et al.*[11] revealed that the TEC between the cathode and electrolyte decreases with B-position Fe doping in $PrBa_{0.5}Sr_{0.5}Co_{1.5}Fe_{0.5}O_{5+\delta}$ (PBSCF) at 0.5, resulting in improved electrochemical performance; however, the chemical compatibility between the two materials was still not matched. Seonhye Park *et al.*[12] prepared a composite cathode material of PBSCF and the electrolyte $Ce_{0.9}Gd_{0.1}O_{1.95}$ (GDC), which can reduce the average TEC. Saccoccio *et al.*[13] reported that doping Nb in PBC benefits its oxygen reduction reaction performance and can

[a]School of Chemistry and Chemical Engineering, Inner Mongolia University of Science and Technology, Baotou 014010, China. E-mail: songboli2021@hotmail.com
[b]School of Rare Earth Industry, Inner Mongolia University of Science and Technology, Baotou, 014010, China
[c]Innovation Center of New Rare Earth Materials Technology, Baotou Research Institute of Rare Earths, Baotou, 014030, China

† Electronic supplementary information (ESI) available. See DOI: https://doi.org/10.1039/d4ra09097g

improve chemical compatibility. When the doping amount of Nb was 0.25, the ASR at 600 °C was reduced to 1.034 Ω cm^2, further enhancing the material's electrochemical performance.

This paper investigates the effect of Co replacement with Nb in PBSCF on its microscopic and electrochemical properties. The electrochemical performance of symmetric and single cells prepared with PBSCFNb_x as the cathode material was studied in detail.

2. Experimental

2.1 Preparation

The $PrBa_{0.5}Sr_{0.5}Co_{1.5-x}Fe_{0.5}Nb_x$ ($x = 0$, 0.02, 0.04, 0.06) materials were prepared *via* the sol–gel method. The raw materials included $Pr(NO_3)_3 \cdot 6H_2O$(AR), $Ba(NO_3)_2$(AR), $Fe(NO_3)_3 \cdot 9H_2O$(AR), $Co(NO_3)_2 \cdot 6H_2O$(AR), $Sr(NO_3)_2$(AR), $Ce(NO_3)_3 \cdot 6H_2O$(AR), $Sm(NO_3)_3 \cdot 6H_2O$(AR), $C_6H_8O_7 \cdot H_2O$(AR), NiO(AR), and $C_{10}H_{16}N_2O_8$(AR). A solution was obtained through dissolution in deionized water at a ratio of metal ion: citric acid (CA): ethylenediaminetetraacetic acid (EDTA) = 1 : 1 : 5 : 2. CA was added, and the mixture was stirred until dissolved. Ammonia and deionized water were mixed in a 1 : 3 ratio and slowly added to a beaker containing EDTA. The EDTA mixed solution was then added to the mixed solution of metal ions and CA, and the pH was adjusted to 7–8 after thorough mixing. The final solution was placed in a water bath at a constant temperature of 80 °C and stirred until it formed a gel. The gel was heated in a box resistance furnace to obtain a fluffy precursor, which was placed in a muffle furnace and kept at 1200 °C for 5 h to acquire the target products, named PBSCFNb_x ($x = 0$, 0.02, 0.04, 0.06). The obtained cathode powder was pressed into cuboid strips in a mold with dimensions of 29.0 mm × 6.0 mm × 0.5 mm at 300 MPa, placed in a muffle furnace, held at 1200 °C for 5 h, and then sintered into dense strips. Conductivity was measured using the four-probe method.

The $Sm_{0.2}Ce_{0.8}O_{1.9}$ (SDC) precursor was prepared using the same method, and SDC powder was obtained after heating the precursor at 800 °C in a muffle furnace for 2 h. The SDC powder was poured into a circular mold (with a diameter of 12 mm), smoothed evenly, pressed at a pressure of 300 MPa to form a round sheet, and placed in the muffle furnace at a temperature rate of 2 °C min^{-1} to 1450 °C for 5 h to obtain the SDC electrolyte sheet. The obtained PBSCFNb_x powder and mixed slurry (ethyl cellulose : terpinol = 6 : 94) were ground into mixed cathode slurry at a ratio of 7 : 3, coated on both sides of the SDC electrolyte sheet, and sintered at 1200 °C in the muffle furnace to obtain a symmetrical cell.

The electrolyte-supported single cell was prepared for testing. The electrolyte sheet, coated with NiO slurry (prepared using the same method as the cathode slurry) on one side, was placed in the muffle furnace at 1300 °C to form a half cell. Then, the other side was coated with cathode slurry, and the single cell was sintered at 1200 °C in the muffle furnace.

2.2 Characterization

The phase composition and crystal structure of the samples were analyzed using an X-ray diffractometer (XRD, Malvern Panalytical, Empyrean) at a scanning rate of 5° min^{-1}, a scanning range of 20°–80°, and Cu Kα radiation (40 kV, 40 mA, $\lambda = 1.5418$ Å). The results were refined using Rietveld methods with GSAS/EXPGUI software. The lattice spacing of the materials was characterized *via* transmission electron microscopy (TEM, FEI Tecnai F20). Energy-dispersive X-ray and high-resolution TEM analyses were performed. The surface element valence was analyzed using X-ray photoelectron spectroscopy (XPS, Thermo Scientific, EscaLab250Xi). A thermal dilatometer (NETZSCH, DIL 420C) was used to test the thermal expansion coefficient (TEC) of the cathode material from 30 °C to 750 °C. The oxygen vacancy of PBSCFNb_x was quantitatively analyzed through electron paramagnetic resonance (EPR, Bruker, EMX PLUS). Scanning electron microscopy (SEM, TESCAN, GAIA3) was used to test the cross-section of the symmetric cell. Electrical conductivity (300–800 °C), electrochemical impedance spectra (EIS, 600–800 °C, 100 kHz–0.1 Hz), and power density (650–800 °C) were tested at 50 °C intervals using an electrochemical workstation (Metrohm, PGSTAT302).

3. Results and discussion

Fig. 1(a) presents the XRD patterns of PBSCFNb_x at room temperature after calcination at 1200 °C for 5 h. According to a comparison of standard XRD patterns, no other diffraction peaks appeared, and the peak positions matched well with those of undoped materials. This finding proves that no other impurities were produced in the prepared cathode materials, and all of them exhibited a single tetragonal structure.[14] Fig. 1(b) shows a partial amplification of the XRD pattern from 32° to 34°. The ionic radius of Nb is 0.64 Å, larger than those of Co^{4+} (0.53 Å) and Co^{3+} (0.61 Å), which increased the cell volume of PBSCF. With the increase in the Nb content, the diffraction peak gradually shifted to a lower angle. Rietveld refinement was used to further study the effect of Nb doping on the crystal structure. Fig. S1 and Table S1† show the Rietveld-refined XRD patterns of PBSCFNb_x. The cell volume increased with an increase in Nb content. TEM and EDS analysis further corroborate these findings on PBSCFN$b_{0.04}$, and the analysis results are shown in Fig. 1(c) and (d), respectively. Each element displayed a uniform distribution with no aggregation. Fig. 1(d) and Table S2† present the elemental analysis results for region 1. Nb was successfully added to PBSCF. The lattice spacing of PBSCF and PBSCFN$b_{0.04}$ was calculated (Fig. 1(c) and (d), respectively). The lattice spacing of 100 crystal planes increased from 0.384 nm to 0.387 nm; this slight increase confirms the successful doping of Nb. The calculated results of lattice spacing were consistent with those obtained by refinement. The Goldschmidt tolerance factor t is used to predict the stability of PBSCFNb_x materials.[15] The calculation results for t are summarized in Table S3.† The results show that the addition of Nb reduces the t of PBSCF, bringing it closer to 1. Therefore, the introduction of Nb to PBSCF improves the thermal stability of the material.

$$t = \frac{r_A + r_O}{\sqrt{2}(r_B + r_O)} \quad (1)$$

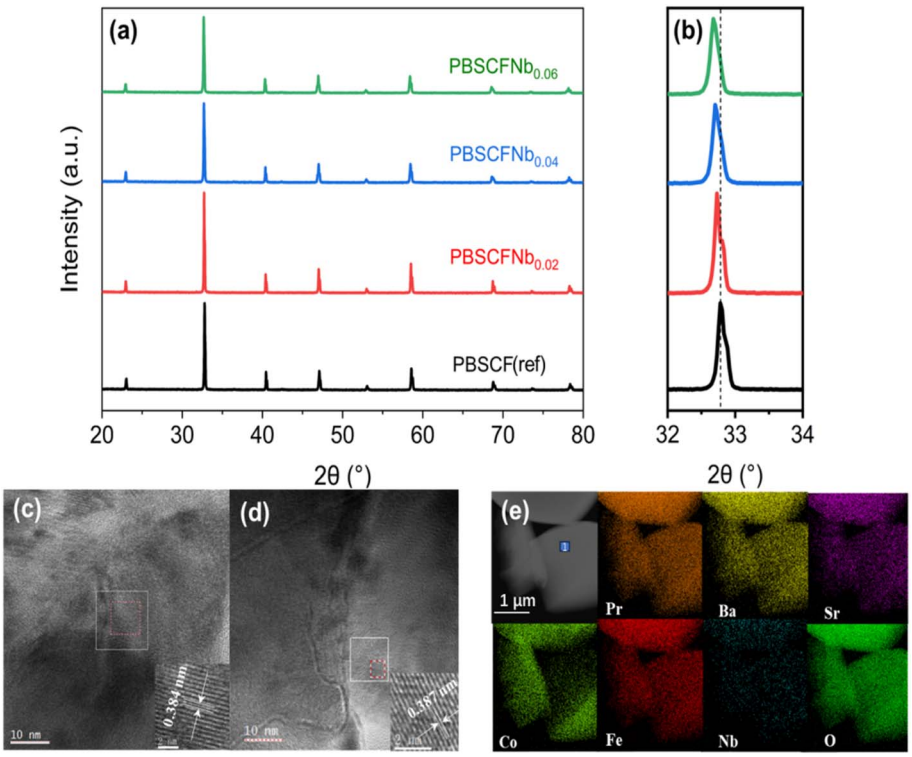

Fig. 1 (a) XRD patterns of PBSCFNb$_x$ cathode materials. (b) Magnified XRD patterns of PBSCFNb$_x$. (c) High-resolution TEM of PBSCF. (d) High-resolution TEM of PBSCFNb$_{0.04}$, and (e) EDS of PBSCFNb$_{0.04}$.

where r_A, r_B, and r_O refer to the average ionic radii of positions A, B, and O, respectively. The ionic radii of each element in PBSCFNb$_x$ are 1.305 Å (Pr^{3+}),1.61 Å (Ba^{2+}), 1.44 Å (Sr^{2+}), 0.61 Å (Co^{3+}), 0.53 Å (Co^{4+}), 0.645 Å (Fe^{3+}), and 0.585 Å (Fe^{4+}).

The TEC of SOFC components should be as close as possible to effectively prevent cell cracking and degradation under high-temperature conditions. Fig. 2 presents the average TEC curve of PBSCFNb$_x$ in an air atmosphere over a temperature range of 30–750 °C. This finding demonstrates that the thermal expansion degree (dL/L_0) in this temperature range decreased with an increasing Nb doping amount, as the bond energy of the Nb–O bond is higher than that of the Co–O bond. When the amount of Nb doping reached 0.06, the average TEC decreased from 21.1 × 10^{-6} K^{-1} to 18.0 × 10^{-6} K^{-1}. Table S4† shows that the addition of Nb greatly improved the average TEC between PBSCFNb$_x$ and the SDC electrolyte, potentially extending the service life of the cell.

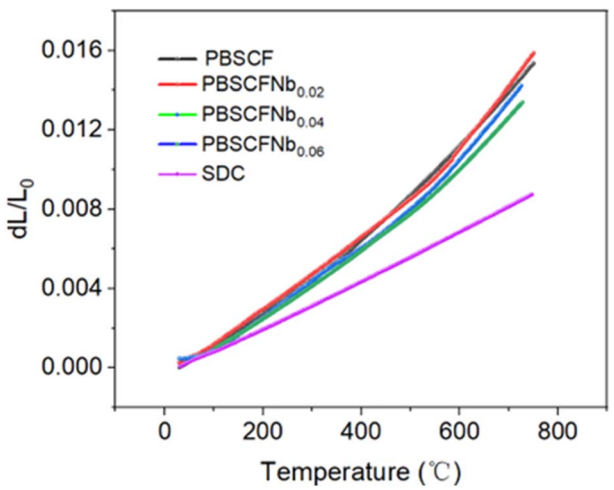

Fig. 2 The thermal expansion of PBSCFNb$_x$ and SDC.

The valence states of surface ions in PBSCFNb$_x$ were analyzed *via* XPS. The peak-fitting results for the O 1s orbit are shown in Fig. 3(a). The activation energy was divided into three oxygen ion states, namely. $O_{adsorbed}$, $O_{lattice}$, and $O_{vacancy}$, from 525 eV to 536 eV.[16] The lattice oxygen at 531.7 eV corresponds to the oxygen state of the perovskite structure, the characteristic peak at 528.3 eV corresponds to chemisorbed oxygen, and the peak at 529.3 eV represents the oxygen vacancy.[17,18] Doping with high-valence elements will reduce the oxygen vacancy concentration. According to the semi-quantitative analysis of XPS, the oxygen vacancy concentration decreases from 20.35% to 13.27% (Table S5†), which coincides with the EPR analysis of oxygen vacancy. The reduction in oxygen vacancy concentration will directly affect cell performance tests. Fig. 3(b) shows the XPS of Fe ions in PBSCFNb$_x$, which lacks symmetry. The peaks at binding energy values of 723.7 and 714.6 eV correspond to Fe^{3+} $2p_{3/2}$ and Fe^{4+} $2p_{3/2}$, respectively.[19–21] Meanwhile, the peaks at 710.8 eV correspond to the spectral peaks of Fe^{3+} $2p_{1/2}$. The absence of Fe^{2+} in the XPS of PBSCFNb$_x$ indicates a high oxidation state of Fe ions. Fe^{4+} was reduced from 15.15% to 3.03% (Table S5†). Fig. 3(c) shows the XPS of Co ion in PBSCFNb$_x$. The binding energy values of 795.3 and 780.4 eV

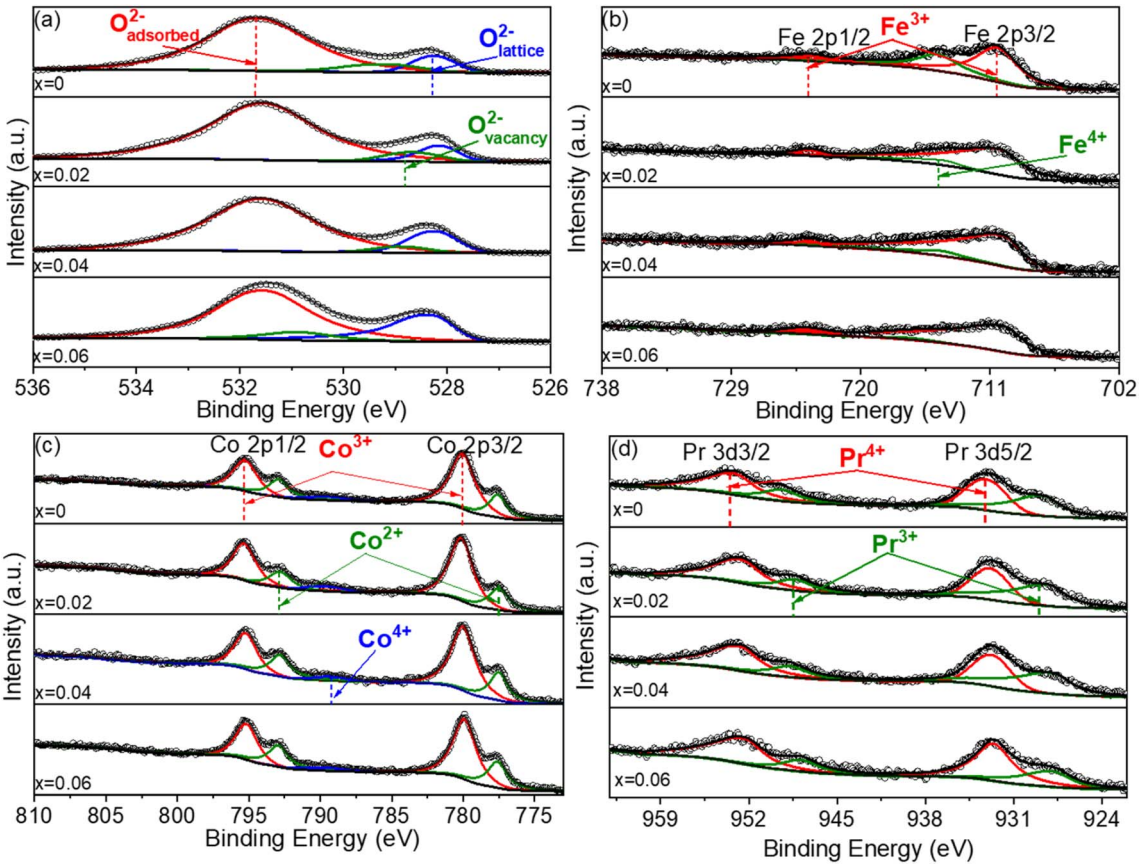

Fig. 3 XPS curves of PBSCFNb$_x$: (a) O 1s, (b) Fe 2p, (c) Co 2p, (d) Pr 2p.

correspond to Co^{3+} $2p_{1/2}$ and Co^{3+} $2p_{3/2}$, respectively. The Co^{2+} $2p_{1/2}$ and Co^{2+} $2p_{3/2}$ spectral peaks in PBSCF had binding energy values of 793.1 and 777.4 eV, respectively. A Co^{4+} spectral peak of 789.8 eV was also observed. The Co in PBSCFNb$_x$ presented three valence distributions.[15,22] According to the principle of electric neutrality, the addition of Nb^{5+} reduces the conversion of Co^{4+} to Co^{3+}. The semi-quantitative analysis of the Co content showed that the doping of Nb reduced the Co^{4+} content from 4.77% to 3.4% (Table S5†), thus influencing the properties of conductivity and thermal expansion. Fig. 3(d) shows the XPS of Pr ions. The spectral peaks of Pr^{4+} $3d_{3/2}$ and Pr^{4+} $3d_{5/2}$ were located at 953.3 and 932.8 eV, respectively. The energy spectra of 948.9 eV and 928.4 eV correspond to Pr^{3+} $3d_{2/3}$ and Pr^{3+} $3d_{5/2}$, respectively, indicating that Pr^{3+} and Pr^{4+} coexist in PBSCF.[23,24] Thus, Fe^{3+}/Fe^{4+}, $Co^{2+}/Co^{3+}/Co^{4+}$, and Pr^{3+}/Pr^{4+} exist in PBSC and PBSCFNb$_{0.04}$, and the presence of mixed oxidation states enhances the oxygen reduction reaction in the cathode materials.

The oxygen vacancy in Nb-doped PBSCF was measured *via* EPR (Fig. 4). The results showed symmetrical oxygen vacancy signal peaks, with symmetrical signals appearing at $g = 2.003$. The peak of oxygen vacancy varied significantly among each sample, mainly because the addition of the high-valency Nb ion reduces the average valency of the other elements, affecting the content of oxygen vacancy. To further study the effect of Nb addition on oxygen vacancy concentration in PBSCF, we conducted quantitative tests on the oxygen vacancy concentration in PBSCFNb$_x$; the results are shown in Table S6.† The oxygen vacancy concentration decreased gradually with the addition of Nb, from 6.936×10^{16} to 3.539×10^{16}. The oxygen vacancy concentration in SOFC affects conductivity, ASR, and power density. Thus, oxygen vacancies serve as channels for O^{2-} transmission in the cathode material and are important indicators of catalytic activity on the cathode surface.[25] The higher the oxygen vacancy concentration, the stronger the oxygen

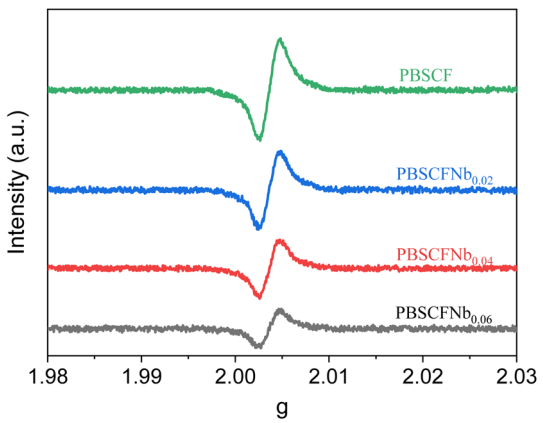

Fig. 4 The oxygen vacancy test curve in PBSCFNb$_x$.

adsorption capability, which aids the oxidation reaction of SOFC. Therefore, the addition of Nb will reduce the surface exchange of oxygen molecules and limit oxygen reduction.

Fig. 5 shows the cross-section microstructure of the symmetrical cell. The symmetric cell had a cathode coating with a porous structure and a dense SDC electrolyte layer. The porous cathode material facilitated oxygen transport and provided a site for the oxygen redox reaction. The compact SDC electrolyte layer was tightly bound to the cathode coating, and the microstructure of the cathode coating did not change noticeably, ensuring the transfer of O^{2-} to the SDC electrolyte at the three-phase interface (TPB). The thickness of the coating also had a certain effect on the performance of the symmetrical cell. The symmetric batteries obtained using each component displayed similar thicknesses, reducing the influence of the cathode thickness on the ASR.

Fig. 6(a) presents the conductivity (σ) test curve of PBSCFNb$_x$ at various temperatures in an air atmosphere. The conductivity increased first and then decreased with temperature. Therefore, PBSCFNb$_x$ is a P-type conductor, and when the temperature was below 400 °C, its conductivity followed a small polarized molecular transition and increased with the temperature. The small polaron transition is represented by the following conductivity model:[11]

$$\sigma = (C/T)\exp(-E_a/kT), \quad (2)$$

where σ represents the electrical conductivity; C denotes the pre-exponential factor unique to the material; T is the temperature under test; E_a indicates the activation energy required for the reaction, and k is the reaction rate constant. When the temperature is below 400 °C, $kT < E_a$, the conductivity depends on the exponential term and increases with temperature. When the temperature exceeds 400 °C, $kT > E_a$, the conductivity depends on the pre-exponential factor term and decreases with increasing temperature. When $kT = E_a$, the conductivity of the material is at its highest. Meanwhile, the electrons in PBSCF are mainly transported by Co^{4+}–O^{2-}–Co^{3+} and Fe^{4+}–O^{2-}–Fe^{3+}, and the conductivity conforms to the small polaron transition at temperatures below 400 °C. At temperatures greater than 400 °C, Fe^{4+} and Co^{4+} reduce to Fe^{3+} and Co^{3+}, respectively, resulting in an increase in oxygen vacancies and hindering the transport of Co^{4+}–O^{2}–Co^{3+} and Fe^{4+}–O^{2-}–Fe^{3+}. The PBSCF reaction can be expressed using eqn (3) and (4). With the progress of the reaction, the oxygen vacancy concentration gradually increased, and the conductivity decreased.[26]

$$2Co^{\cdot}_{Co} + O^{\times}_{O} \rightarrow 2Co^{\times}_{Co} + V^{\cdot\cdot}_{O} + \frac{1}{2}O_2, \quad (3)$$

$$2Fe^{\cdot}_{Fe} + O^{\times}_{O} \rightarrow 2Fe^{\times}_{Fe} + V^{\cdot\cdot}_{O} + \frac{1}{2}O_2, \quad (4)$$

where $O^{\times}_{O}$ and $V^{\cdot\cdot}_{O}$ are the lattice oxygen and oxygen vacancy, respectively. Fig. 6(b) shows the relationship between Nb content and conductivity at 400 °C. All materials reached their maximum value at 400 °C, with conductivities at $x = 0$, 0.02, 0.04, and 0.06 being 1111.72, 1004.54, 986.81, and 808.92 S cm^{-1} (errors due to conductivity fitting are shown in Table S7†), respectively. It can be seen from TEM that the addition of Nb causes lattice distortion in PBSCF, evidenced by the lattice constants. The XRD refinement results indicate that the lattice constant gradually increases, the lattice barrier decreases, and the oxygen vacancy concentration decreases, suggesting that conductivity should increase. However, in perovskite materials, carriers predominantly transmit through the B–O–B structure. Some Co–O bonds are replaced by longer Nb–O bonds, lengthening the carrier transmission path, and decreasing the carrier migration rate. According to the principle of charge conservation and XPS analysis, it can be concluded that B-position Nb doping leads to an increase in non-conductive Nb–O bonds, reducing the spin of Co^{4+} to Co^{3+}, which is the main reason for the higher conductivity of cobalt-based materials, and thus, the electron conductivity decreases. When Co and Fe coexisted, the ion compensation mechanism showed that Fe^{4+} preferentially obtained electrons compared to Co^{4+}.[27] However, the addition of Nb in this experiment inhibited the increase in the content of Fe^{4+}. In contrast to the system where Co and Fe coexisted, Co^{4+} obtained electrons more easily, promoting the stabilization of high spin states of Co and Fe, which led to a decrease in conductivity. Based on the Arrhenius diagram in Fig. 6(a) and the small polaron transition model, the activation energy and pre-exponential factor of the material at the maximum conductivity were obtained (Fig. 6(c) and (d)). The pre-exponential factor of the material itself gradually decreased with the doping of Nb. The activation energy increased, and conductivity decreased with the rising Nb content at 400 °C.

Based on the Alder theory, the equivalent circuit diagrams in Fig. 7(a)–(c) were established. In the circuit, L represents the inductance generated by the test device and the electrode lead, and R_s is the ohmic resistance from the cathode, the Pt line, the

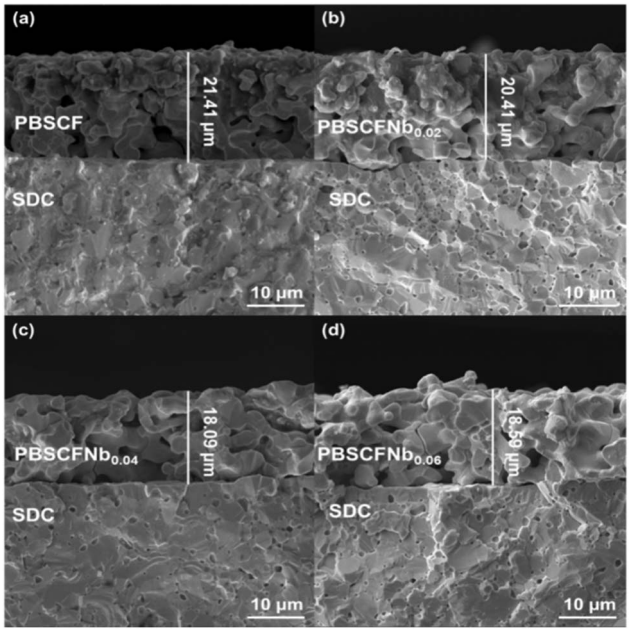

Fig. 5 Cross-section of SEM images of (a) PBSCF, (b) PBSCFNb$_{0.02}$, (c) PBSCFNb$_{0.04}$, and (d) PBSCFNb$_{0.06}$.

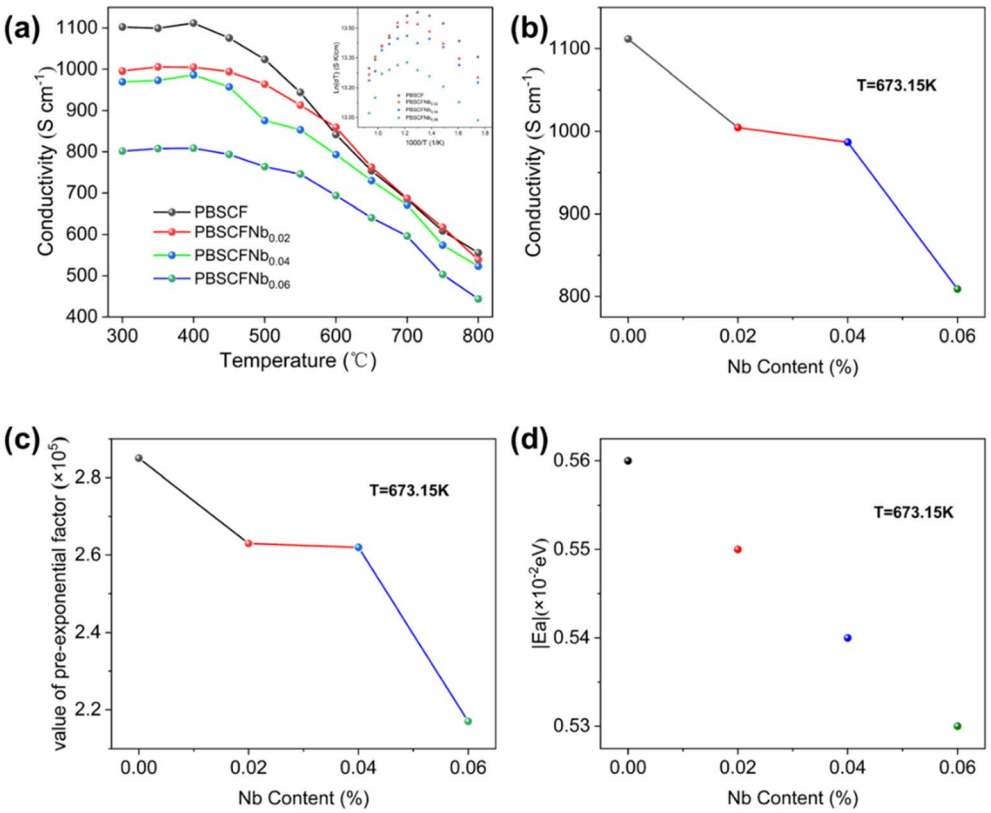

Fig. 6 (a) The change of conductivity with temperature and the relation between Arrhenius and conductivity. (b) The relation between conductivity and Nb content at 400 °C. (c) The relation between pre-exponential C and Nb content at 400 °C. (d) The relation between E_a and Nb content at 400 °C.

contact between the electrolyte and the cathode, and the electrolyte. The main role is the contact resistance between the cathode layer and the electrolyte. R_{HF} and R_{LF} refer to mid-frequency and low-frequency polarization resistors, while CPE1 and CPE2 are constant-phase elements corresponding to each frequency range.[28] The ASR values of PBSCF and PBSCFNb$_{0.04}$ decreased with increasing temperature because Co^{4+} and Fe^{4+} in PBSCF underwent reduction reactions in a high-temperature environment, leading to lower valence states, increased oxygen vacancy concentration, and decreased ASR. Fig. 7(c) and (d) show the ASR diagrams of PBSCFN$_x$ at 800 °C and PBSCFN$_x$ with different Nb content, respectively. At the same temperature, the ASR decreased with increasing Nb content, although it increased when the doping level was raised to 0.06 Nb. At 800 °C with a doping amount of 0.04, the ASR reached its minimum at 0.0336 Ω cm^2. The ASR is closely related to the oxygen vacancy concentration, but it can be seen from Fig. 7(c) and (d) that as the oxygen vacancy concentration decreases, the ASR value decreases, instead of increasing. The phenomenon can be attributed to the fact that R_{HF} is related to the migration of oxygen ions, while R_{LF} is related to the adsorption, dissociation, and diffusion of oxygen in the oxygen reduction reaction (ORR). The calculations for R_{HF} and R_{LF} are as follows (R_{HF}: PBSCF, PBSCFNb$_{0.02}$, PBSCFNb$_{0.04}$, PBSCFNb$_{0.06}$ are 0.0247, 0.0123, 0.0109 and 0.0172 Ω, respectively, R_{LF}: PBSCF, PBSCFNb$_{0.02}$, PBSCFNb$_{0.04}$, PBSCFNb$_{0.06}$ are 0.0246, 0.0232, 0.0227, 0.0238 Ω, respectively). Errors due to ASR fitting are shown in Table S8.† R_{HF} and R_{LF} demonstrated a trend of decreasing and then increasing. However, the decrease in R_{LF} indicated that the oxygen surface exchange performance improved with the doping of Nb. The increase in oxygen vacancy concentration led to defect association of the material, which caused oxygen vacancy localization.[29] The distribution of relaxation time (DRT) analysis results of the PBSCFNbx series materials is shown in Fig. S2.† The results indicate that, in the high-frequency region, the impedance (R_{HF}) shows a pattern of first increasing and then decreasing, consistent with the pattern in Fig. 8(c). From $x = 0$ to 0.04, the peak width of the high-frequency peak gradually increases, indicating that the time for oxygen ions to transition from the reaction transient state to the steady state becomes shorter, improving the chemical reaction kinetics and accelerating the reception and escape speed of oxygen ions,[30,31] thereby increasing the chemical reaction rate of the material. When $x =$ 0.06, the peak width decreases, the oxygen ion transference number reduces, and the impedance increases. Table 1 shows that the ASR value of PBSCFNb$_{0.04}$ is considerably lower than that reported in the literature.

To investigate the effect of PBSCFNb$_x$ as a SOFC cathode on power density, we prepared an electrolyte-supported single cell. Fig. 8(a) and (b) display the power density of PBSCF and PBSCFNb$_{0.04}$ in a hydrogen atmosphere from 650 °C to 800 °C. The power density increased with temperature due to the

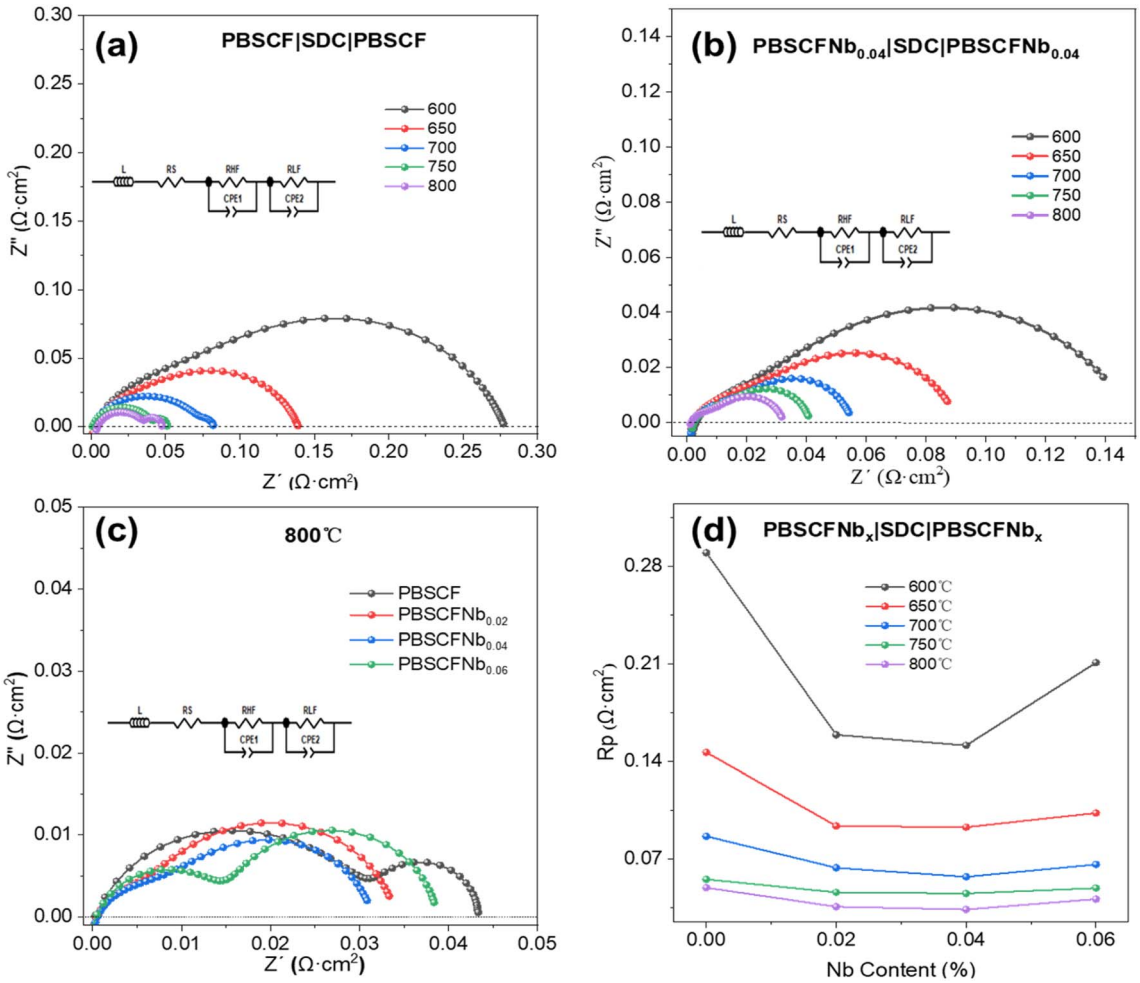

Fig. 7 ASR shows the temperature dependence of (a)PBSCF, (b) $PBSCFNb_{0.04}$, (d)$PBSCFNb_x$, and an (c) ASR diagram of $PBSCFNb_x$ at 800 °C.

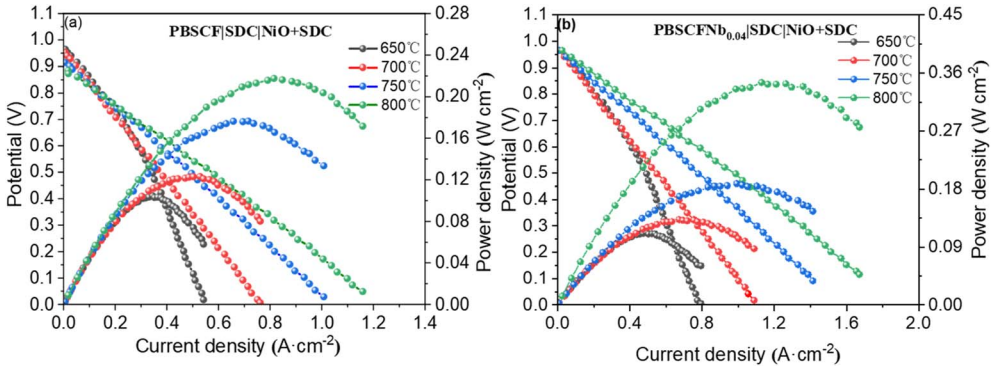

Fig. 8 (a) The power density of a single cell PBSCF|SDC|Ni + SDC at 650–800 °C and (b) the power density of single cell $PBSCF_{0.04}$|SDC|Ni + SDC at 650–800 °C.

acceleration of oxygen ion transport and gas diffusion as the temperature rose. At 650 °C, the open-circuit voltage values were 0.91 and 0.98 V, all lower than the theoretical voltage of 1.1 V because SDC has a certain N-type electronic conductivity.[34] Furthermore, a portion of Ce^{4+} was reduced to Ce^{3+} under a high-temperature reduction atmosphere, resulting in a lower voltage. The power density of the single cell prepared using PBSCF at 800 °C was 217.7 mW cm^{-2}, while that prepared with $PBSCFNb_{0.04}$ was 328.3 mW cm^{-2}, indicating an increase of 110.6 mW cm^{-2}. This finding was observed because the power density of a single cell increases as the ASR value of a symmetrical cell decreases.

Table 1 The ASR of other Co-based materials R_p (Ω cm^2)

Sample	Temperature (°C)	R_p (Ω cm^2)	Ref.
LnBaCo	800	0.046	18
PBCF	800	0.049	32
PBSCF	800	0.067	15
PBSCFNb$_{0.04}$	800	0.034	This work
PBSCFNb$_{0.04}$	700	0.057	This work
PBCM	700	0.067	33

4. Conclusion

A series of materials PBSCFNb$_x$ (x = 0, 0.02, 0.04, 0.06) was prepared as cathode materials for SOFC *via* the sol–gel method, and all of them exhibited a single tetragonal structure. With the increase of Nb content, the oxygen vacancy concentration decreased, but the exchange performance of the oxygen surface was effectively improved and the ASR was reduced. The TEC of PBSCFNb$_{0.04}$ decreased from 21.1 $\times$ 10^{-6} K^{-1} to 18.0 $\times$ 10^{-6} K^{-1}, which effectively reduced the thermal expansion of the material. At 800 °C, the power density of PBSCFNb$_{0.04}$ increased by 110.6 mW cm^{-2}. The ASR reached a minimum of 0.0336 Ω cm^2 at x = 0.04, implying its potential as a SOFC cathode material.

Data availability

The data are available from the corresponding author upon reasonable request.

Conflicts of interest

There are no conflicts to declare.

Acknowledgements

The work was supported by the Inner Mongolia Autonomous Region universities' basic scientific research project (2023CXPT002), the Baotou Science and Technology Bureau project (YF2022014), the Open Research Project for Innovation Center of New Rare Earth Materials Technology (CXZX-D-202409-0020), and the integrated research platform for novel and important energy comprehensive utilization technology in Inner Mongolia Autonomous Region.

References

1 T. Hai, H. Almujibah, L. Mostafa, J. Kumar, T. Van Thuong, B. Farhang, M. H. Mahmoud and W. El-Shafai, *Int. J. Hydrogen Energy*, 2024, **63**, 193–206.
2 S. Hu, J. Li, Y. Zeng, J. Pu and B. Chi, *Phys. Chem. Chem. Phys.*, 2023, **25**, 5926–5941.
3 A. Ndubuisi, S. Abouali, K. Singh and V. Thangadurai, *J. Mater. Chem. A*, 2022, **10**, 2196–2227.
4 J. Li, Q. Cai and B. Amini Horri, *Mater. Adv.*, 2025, **6**, 39–83.
5 F. Lu, Y. Shi, L. Shi, M. Li, R. Cui, J. Wang, H. He, J. Su, J. Wang and B. Cai, *Ceram. Int.*, 2024, **50**, 46318–46326.
6 S. Park, S. Choi, J. Shin and G. Kim, *J. Power Sources*, 2012, **210**, 172–177.
7 S. Lü, G. Long, X. Meng, Y. Ji, B. Lü and H. Zhao, *Int. J. Hydrogen Energy*, 2012, **37**, 5914–5919.
8 Y. Liu, F. Han, H. Xia, Z. Zhang, Q. Zhou, B. Xu and H. Shi, *Ceram. Int.*, 2024, **50**, 52904–52916.
9 S. Lü, Y. Zhu, X. Fu, R. Huang, Y. Guo, W. Zhang, H. Li, L. Hou and X. Meng, *J. Alloys Compd.*, 2022, **911**, 165002.
10 J. Zou, J. Park, B. Kwak, H. Yoon and J. Chung, *Solid State Ionics*, 2012, **206**, 112–119.
11 H. Bai, Z. Leng, T. Chen, B. Zhang, J. Chu, Y. Zhang, Q. Zhou, J. Zhou and S. Wang, *Int. J. Hydrogen Energy*, 2023, **48**, 23655–23669.
12 S. Park, S. Choi, J. Shin and G. Kim, *RSC Adv.*, 2014, **4**, 1775–1781.
13 M. Saccoccio, C. Jiang, Y. Gao, D. Chen and F. Ciucci, *Int. J. Hydrogen Energy*, 2017, **42**, 19204–19215.
14 J. Li, Q. Zhang, P. Qiu, L. Jia, B. Chi, J. Pu and J. Li, *J. Power Sources*, 2017, **342**, 623–628.
15 J. Zan, S. Wang, D. Zheng, F. Li, W. Chen, Q. Pei and L. Jiang, *Mater. Res. Bull.*, 2021, **137**, 111173.
16 W. Jia, Z. Huang, W. Sun, L. Wu, L. Zheng, Y. Wang, J. Huang, X. Yang, M. Lv and L. Ge, *J. Power Sources*, 2021, **490**, 229564.
17 F. He, F. Zhu, D. Liu, Y. Zhou, K. Sasaki, Y. Choi, M. Liu and Y. Chen, *Mater. Today*, 2023, **63**, 89–98.
18 S. Wang, J. Zan, W. Qiu, D. Zheng, F. Li, W. Chen, Q. Pei and L. Jiang, *J. Electroanal. Chem.*, 2021, **886**, 115144.
19 M. Liang, Y. Song, D. Liu, L. Xu, M. Xu, G. Yang, W. Wang, W. Zhou, R. Ran and Z. Shao, *Appl. Catal.*, 2022, **318**, 121868.
20 J. Gao, Q. Li, Z. Zhang, Z. Lü and B. Wei, *Electrochem. Commun.*, 2021, **125**, 106978.
21 J. Gao, Y. Liu, Y. Gao, M. Yuan, Z. Wang, Z. Lü, Q. Li and B. Wei, *Chem. Eng. J.*, 2023, **452**, 139584.
22 Y. Kim, H. Schlegl, K. Kim, J. T. S. Irvine and J. H. Kim, *Appl. Surf. Sci.*, 2014, **288**, 695–701.
23 W. Xia, X. Liu, F. Jin, X. Jia, Y. Shen and J. Li, *Electrochim. Acta*, 2020, **364**, 137274.
24 Y.-j. Gong, R.-g. He, G.-l. Zhao, L.-j. Jia, J.-y. Gao, F. Wang, K.-j. Duan, T.-c. Liu and J. Fuel, *Chem. Technol.*, 2023, **51**, 996–1005.
25 B. Admasu Beshiwork, X. Wan, M. Xu, H. Guo, B. Sirak Teketel, Y. Chen, J. Song Chen, T. Li and E. Traversa, *J. Energy Chem.*, 2024, **88**, 306–316.
26 M. Chen, H. Zhang, C. Yao, H. Lou, B. Xia, Z. Zhang, Y. Sun, X. Lang and K. Cai, *J. Alloys Compd.*, 2023, **968**, 172084.
27 G. H. Jonker, *Physica*, 1954, **20**, 1118–1122.
28 S. B. Adler, B. T. Henderson, M. A. Wilson, D. M. Taylor and R. E. Richards, *Solid State Ionics*, 2000, **134**, 35–42.
29 Y. N. Kim, J. H. Kim and A. Manthiram, *J. Power Sources*, 2010, **195**, 6411–6419.

30 Z. Han, H. Dong, Y. Wang, Y. Yang, H. Yu and Z. Yang, *J. Mater. Chem. A*, 2023, **11**, 18820–18831.
31 J. H. Kim, K. Jang, D.-K. Lim, S. Ahn, D. Oh, H. Kim, J. Seo, P.-P. Choi and W. Jung, *J. Mater. Chem. A*, 2022, **10**, 2496–2508.
32 F. Jin, H. Xu, W. Long, Y. Shen and T. He, *J. Power Sources*, 2013, **243**, 10–18.
33 J. Xu, H. Cai, G. Hao, L. Zhang, Z. Song, W. Long, L. Zhang and L. Wang, *J. Alloys Compd.*, 2020, **842**, 155600.
34 Z. Han, J. Bai, X. Chen, X. Zhu and D. Zhou, *Int. J. Hydrogen Energy*, 2021, **46**, 11894–11907.